Climate
of the Past
Discussions

1   **Glacial to interglacial climate variability in the southeastern African subtropics (25- 20°S)**

2   Annette Hahn[1], Enno Schefuß[1], Jeroen Groeneveld[1,2], Charlotte Miller[1*], Matthias Zabel[1],

3   [1]MARUM - Center for Marine Environmental Sciences, University of Bremen, Bremen, Germany

4   [2]Alfred Wegener Institute, Helmholtz Center for Polar and Marine Research, Potsdam, Germany

5   *Present address: Leeds Trinity University, Brownberrie Ln, Horsforth, Leeds, LS18 5HD, United Kingdom

6   Contact: ahahn@marum.de

7

8   Abstract

9   We present a continuous and well-resolved record of climatic variability for the past 100,000 yrs

10   from a marine sediment core taken in Delagoa Bight, off southeastern Africa. In addition to

11   providing a sea surface temperature reconstruction for the past ca. 100,000 yrs, this record also

12   allows a high-resolution continental climatic reconstruction. Climate sensitive organic proxies,

13   like the distribution and isotopic composition of plant-wax lipids as well as elemental indicators

14   for fluvial input and weathering type provide information on climatic changes in the adjacent

15   catchment areas (Incomati, Matola, and Lusutfu rivers). At the transition between glacials and

16   interglacials, shifts in vegetation correlate with changes in sea surface temperature in the

17   Agulhas current. The local hydrology, however, does not follow these orbital-paced shifts.

18   Instead, precipitation patterns follow millennial scale variations with different forcing

19   mechanisms in glacial versus interglacial climatic states. During glacials, southward

20   displacement of the Intertropical Convergence Zone facilitates a transmission of northern

21   hemispheric signals (e.g. Heinrich events) to the southern hemispheric subtropics. Furthermore,

22   the southern hemispheric westerlies become a more direct source of precipitation as they shift

23   northward over the study site, especially during Antarctic cold phases. During interglacials, the

24   observed short-term hydrological variability is also a function of Antarctic climate variability,

25   however, it is driven by the indirect influence of the southern hemispheric westerlies and the

26   associated South African high-pressure cell blocking the South Indian Ocean Convergence Zone

27   related precipitation. As a consequence of the interplay of these effects, small scale climatic

28   zones exist. We propose a conceptual model describing latitudinal shifts of these zones along

29   the southeastern African coast as tropical and temperate climate systems shift over glacial and

30   interglacial cycles. The proposed model explains some of the apparent contradictions between

31   several paleoclimate records in the region.

32

33 Key words: Delagoa Bight; southern hemisphere westerlies; South Indian Ocean Convergence

34 Zone; sea surface temperatures; hydrogen isotopes; carbon isotopes; elemental composition

35

36 1.   Introduction

37 Despite the increasing number of southern African paleoclimate studies, large data gaps and

38 unresolved debates remain. Controversies concern both the interpretation of the climate

39 records as well as the contradictory major climate forcings that have been proposed for the

40 region. In southeastern Africa, the main moisture source is the warm Indian Ocean (Tyson and

41 Preston-Whyte, 2000), the mechanisms controlling the intensity and duration of the easterly

42 rainfall over time remain, however, uncertain. Climate variations on glacial-interglacial

43 timescales in southernmost Africa were reported to be directly forced by local (southern

44 hemispheric) insolation (Partridge et al., 1997; Schefuß et al., 2011; Simon et al., 2015; Caley et

45 al., 2018). Strong southern hemispheric summer insolation was hypothesized to cause wet

46 climatic conditions along the east African coast due to a stronger atmospheric convection and

47 an increase in the land/ocean temperature contrast, which results in higher moisture transport

48 by the tropical easterlies. However, recent paleo-reconstructions suggested a synchrony with

49 northern hemisphere climate signals, which are inversely correlated to southern hemispheric

50 insolation (e.g. Truc et al., 2013). As a mechanism of transmitting the northern hemispheric

51 signal to southern Africa, ocean circulation variability (Agulhas current strength; i.e. sea surface

52 temperatures [SST]) has often been proposed (Biastoch et al., 1999; Reason and Rouault, 2005;

53 Dupont et al., 2011; Tierney et al., 2008; Stager et al., 2011; Scott et al., 2012; Truc et al., 2013;

54 Baker et al., 2017; Chase et al., 2017). In terms of vegetation shifts, atmospheric CO_2 variability

55 and temperature have been suggested as major driving mechanisms over glacial-interglacial

56 cycles (Dupont et al., 2019). Nowadays, eastern South Africa is not under the direct influence of

57 the intertropical convergence zone (ITCZ) as its modern maximum southern extension is ca. 13-

58 14°S (Gasse et al., 2008). However, the position of the ITCZ was more southerly during glacial

59 periods (Nicholson and Flohn, 1980; Chiang et al., 2003; Chiang and Bitz, 2005), which may have

60 allowed ITCZ shifts to reach much further south along the east African coast than today (c.f.

61 Johnson et al., 2002; Schefuß et al., 2011; Ziegler et al., 2013; Simon et al., 2015). At the same

Climate
of the Past

Discussions

62   time, the southern hemispheric westerlies (SHW), which presently influence only the

63   southernmost tip of Africa, are hypothesized to have moved northward during glacial periods of

64   increased south Atlantic sea ice extent (Anderson et al., 2009; Sigman et al., 2010; Miller et al.,

65   2019b). As suggested by Miller et al., (2019b), in such a scenario the temperate systems may

66   have brought winterly moisture to the southeast African coast and/or blocked South Indian

67   Ocean Convergence Zone (SIOCZ) related precipitation during the summer months. Regional

68   studies integrating many of the available records have found that; i) several small-scale climatic

69   dipoles exist due to the interaction of various driving mechanisms and that ii) the spatial extent

70   of these climatic regions has varied considerably since the last Glacial (Chevalier et al., 2017,

71   Chase et al., 2018; Miller et al., 2019b). Miller et al., (2019b) compile paleorecords along the

72   southeastern African coast and propose a conceptual model of climatic variability during the

73   Holocene. The authors describe three climatic zones; a *northern SRZ* where the climate is driven

74   by local insolation, and *a central and eastern SRZ* and *southern South African* zone where

75   climate is driven by shifts of the southern hemisphere westerlies, the South African high-

76   pressure cell and the South Indian Ocean Convergence Zone (SIOCZ). Equatorward shifts of the

77   southern hemisphere westerlies, the South African high-pressure cell and the SIOCZ result in

78   humid conditions in the *southern South African zone*, whereas they cause arid conditions in the

79   *central and eastern SRZ.* We analyze a marine core located within the *central and eastern SRZ*

80   that offers a continuous high-resolution record of the past ca. 100,000 yrs allowing us to add to

81   the existing conceptual models of southeastern African climate dynamics, and to gain an

82   understanding of glacial climate mechanisms in the region. A combination of organic and

83   inorganic geochemical proxies is used in order to decipher the hydrological processes on land,

84   while foraminiferal shell geochemistry serves as a proxy for ocean circulation variability. With

85   this approach we aim to decipher some of the discrepancies concerning the driving mechanisms

86   of southeast African hydroclimate and vegetation shifts during the last glacial-interglacial cycle.

87   1.2 Regional setting

88   The coring site is located in an embayment on the southeastern African continental shelf called

89   the Delagoa Bight (Fig. 1). The southern directed Agulhas Current flows along the East African

90   margin transporting warm and saline water from the tropical Indian Ocean to the tip of

91   Southern Africa (Zahn et al., 2012). The current system is structured into a series of large-scale

92   (~200 km diameter) anti-cyclonic eddies occurring about 4 to 5 times per year (Quartly and

Climate
of the Past
Discussions
EGU
Open Access

93   Srokosz, 2004). As they pass the Delagoa Bight, these eddies, together with the Agulhas Current

94   itself, drive the Delagoa Bight eddy; a topographically constrained cyclonic lee eddy at the

95   coring location (Lutjeharms and Da Silva, 1988; Quartly and Srokosz, 2004). Although the coring

96   site is located just west of the mouth of the major Limpopo river system, Schüürman et al.,

97   (2019) show that the inorganic material at our site most likely originates from three minor

98   rivers, Incomati, Matola, and Lusutfu, that flow into the Indian Ocean further to the southwest.

99   This is attributed to the eastward deflection of the Limpopo sediments by the Delagoa Bight

100 eddy. The eddy appears to have been stable and strong enough to effectively constrain the drift

101 of the Limpopo sediments eastwards over the late Pleistocene and Holocene (Schüürman et al.,

102 2019). The three rivers, Incomati (also known as Komati), Matola (also known as Umbeluzi), and

103 Lusutfu (also known as Maputo), have catchment areas of ca. 45 300 km^2, 6 600 km^2, and 22

104 700 km^2, respectively, comprising the coastal region and the eastern flank of the Drakensberg

105 Mountains. Between the Drakensberg escarpment and the coast lies a N-S oriented low ridge,

106 the Lebombo Mountains (400–800 m a.s.l.). The geological formations of this area are the

107 Archaean Kaapvaal Craton, the Karoo Igneous Province, as well as the Quaternary deposits on

108 the coastal plains (de Wit et al., 1992; Sweeney et al., 1994). Climatically these catchments are

109 in the transition zone between tropical and subtropical climate; at the southern limit of the

110 subtropical ridge between the southern Hadley and the Ferrel cell (Tyson and Preston-Whyte,

111 2000). The average annual temperature ranges from 16°C in the highlands to 24°C in the

112 lowland area. (Kersberg, 1996). Rain (ca. 1,000 mm annually) falls mostly in summer (ca. 67 % of

113 annual rainfall from November to March) (Xie and Arkin, 1997; Chase and Meadows, 2007).

114 When the ITCZ is in its southernmost (summer) position, rainfall associated with tropical

115 temperate troughs (TTTs), forming at the SIOCZ bringing warm and humid air from the Indian

116 Ocean (Jury et al., 1993; Reason and Mulenga, 1999) is most intense over our study area.

117 Winter rain (33 % of annual rainfall from April to October) is associated with extratropical cloud

118 bands and thunderstorms linked to low pressure systems that develop in the main SHW flow

119 (between 40 °S and 50 °S) and become cut off and displaced equatorward as far north as 25°S

120 (c.f. Baray et al., 2003; Mason and Jury, 1997). Associated with this climatological and

121 topographic setting we find a vegetation in the Incomati, Matola, and Lusutfu catchment areas

122 that consists mainly of coastal forests and mountain woodlands with savanna elements only in

123 the northernmost parts of the catchment and sedges along the riverbanks and floodplains (see

124   White, (1983) and Dupont et al., (2011) for a more detailed description of the vegetation

125   biomes).

126   2 Material and methods

127   2.1 Sediments

128   Gravity core GeoB20616-1 (958 cm long) was retrieved from 25°35.395′S; 33°20.084′E on

129   15.02.2016 from a water depth of about 460 m. Shipboard sedimentological analysis showed a

130   lithology of clayey silt with signs of slight bioturbation. The composition was observed as mainly

131   clastic with occurrence of foraminifera and shell fragments (Zabel, 2016).

132   2.2 Oxygen isotopic composition of planktonic foraminifera

133   Stable oxygen isotopes values values of planktonic foraminifera (*G. ruber*, white variety, >150 µm)

134   were measured in the interval between 395 and 935 cm at 10 cm resolution for age-modeling

135   (Suppl.1). For each measurement, around eight shells of *G. ruber* were selected and analyzed at

136   the MARUM – Center for Marine Environmental Sciences, University of Bremen, Germany using

137   a ThermoFisher Scientific 253 plus gas isotope ratio mass spectrometer with Kiel IV automated

138   carbonate preparation device. Data were calibrated against an in-house standard (Solnhofen

139   limestone). The results are reported in per mil (‰, parts per thousand) versus Vienna Peedee

140   belemnite (VPDB). Standard deviation of in-house standard (Solnhofen limestone) δ^{18}O over the

141   measurement period was 0.06 ‰.

142   2.3 Age model

143   Until the limit of radiocarbon dating the age model used in this study is based on 8 radiocarbon

144   ages of *G. ruber*, one shell fragment and a bulk total organic carbon surface sample (see Table

145   1). The cleaning procedures as well as the Accelerator Mass Spectrometry (AMS) measurements

146   were carried out in the Poznań Radiocarbon Laboratory, Poland. The modelled ocean average

147   curve (Marine13) (Reimer et al., 2013) and a local marine ΔR of 121±16 ^{14}C yr (Maboya et al.,

148   2017) were applied to calibrate the radiocarbon ages. To perform these calculations the Calib

149   7.1 software (Stuiver et al., 2019) was used. For flexible Bayesian age-depth modelling of the

150   available C^{14} dates, the software Bacon (Blaauw and Christen, 2011) (Fig 2b) was used. The age-

151   depth model was extended by planktonic foraminifera δ^{18}O correlation using the δ^{18}O shifts in

152 the LR04 stack as a reference (Lisiecki and Raymo, 2005) (Fig. 2a,b). The calibrated ^{14}C age of a

153 shell fragment found in this interval was used as a ^{14}C-tie-point (see Table 1), additionally 2 δ^{18}O

154 tie-points were defined and an age model was calculated using the time series tuning software

155 AnalySeries (Paillard et al., 1996) (Fig. 2a). In order to estimate the error of δ^{18}O tie-points the

156 mean resolution of the GeoB20616-1 benthic δ^{18}O record and the reference curve around the

157 tie-point depth and age (respectively) was taken into account as well as the absolute age error

158 of the time-scale used for the reference record and a matching error visually estimated when

159 defining tie-points. The uncertainty of the radiocarbon dates is indicated in Table 1. In this

160 paper, we refer to median age estimations; the uncertainty of the model is indicated in Fig. 2b

161 (grey lines).

162 2.4 Foraminiferal Mg/Ca

163 Up to 20 specimens (> 150 µm) of *G. ruber* (white) (> 150 µm) were selected for Mg/Ca analysis

164 (see Suppl.2). Foraminiferal tests were gently crushed prior to standard cleaning procedures for

165 Mg/Ca in foraminifera (Barker et al., 2003). For clay and organic matter removal ultrasonic

166 cleaning was alternated with washes in deionized water and methanol, an oxidizing step with 1

167 %-H_2O_2 buffered in 0.1M NaOH followed, which was then neutralized by deionized water

168 washes. A final weak acid leach with 0.001M QD HNO_3 was performed before dissolution in

169 0.5 mL 0.075 M QD HNO_3 and centrifugation for 10 min (6,000 rpm). The samples were diluted

170 with Seralpur water before analysis with inductively coupled plasma optical emission

171 spectrometry (Agilent Technologies, 700 Series with autosampler ASX-520 CETAC and micro-

172 nebulizer) at MARUM, University of Bremen, Germany. Instrumental precision was monitored

173 after every five samples using analysis of an in-house standard solution with a Mg/Ca of 2.93

174 mmol mol^{-1} (standard deviation of 0.020 mmol mol^{-1} or 0.67 %). A limestone standard

175 (ECRM752-1, reported Mg/Ca of 3.75 mmol mol^{-1}) was analyzed to allow inter-laboratory

176 comparison (Greaves et al., 2008; Groeneveld and Filipsson, 2013).

177 2.5 Organic geochemistry

178 Total lipid extracts (TLEs) were extracted from ca. 9-27 g of the freeze-dried, homogenized

179 samples with a DIONEX Accelerated Solvent Extractor (ASE 200) at 100°C and at 1,000 psi for 5

180 minutes (repeated 3 times) using a dichloromethane (DCM):methanol (MeOH) (9:1, v/v)

181 mixture. Squalane was added in a known amount to the samples as internal standard before

182   extraction. Elemental sulphur was removed from the TLEs using copper turnings. After

183   saponification by adding 6 % KOH in MeOH and extraction of the neutral fractions with hexane,

184   the neutral fractions were split into hydrocarbon, ketone, and polar fractions using silica gel

185   column chromatography (with a mesh size of 60 µm) and elution with hexane, DCM and

186   DCM:MeOH (1:1), respectively. Subsequently elution of the hydrocarbon fractions with hexane

187   over an $AgNO_3$-impregnated silica column yielded saturated hydrocarbon fractions. The

188   concentrations of long-chain n-alkanes in the saturated hydrocarbon fractions were determined

189   using a Thermo Fischer Scientific Focus gas-chromatograph (GC) with flame-ionization-detection

190   (FID) equipped with a Restek Rxi 5ms column (30m x 0.25mm x 0.25µm). Quantities of

191   individual n-alkanes were estimated by comparison with an external standard containing n-

192   alkanes (C_{19}–C_{34}) at a known concentration. Replicate analyses of the external standard yielded

193   a quantification uncertainty of <5 %. The carbon preference index (CPI) was calculated using the

194   following equation:

195   CPI = 0.5 * ($\sum C_{odd27-33}/ \sum C_{even26-32} + \sum C_{odd27-33}/ \sum C_{even28-34}$) with C_x the amount of each

196   homologue (Bray and Evans 1961).

197   The δD values of long-chain n-alkanes were measured using a Thermo Trace GC equipped with

198   an Agilent DB-5MS (30m length, 0.25 mm ID, 1.00 µm film) coupled via a pyrolysis reactor

199   (operated at 1420°C) to a Thermo Fisher MAT 253 isotope ratio mass spectrometer (GC/IR-MS).

200   The δD values were calibrated against external H_2 reference gas. The H^{3+} factor was monitored

201   daily and varied around 6.23 ± 0.04 ppm nA^{-1}. δD values are reported in permil (‰) versus

202   Vienna Standard Mean Ocean Water (VSMOW). An n-alkane standard of 16 externally calibrated

203   alkanes was measured every 6th measurement. Long-term precision and accuracy of the

204   external alkane standard were 3 and <1 ‰, respectively. When n-alkane concentrations

205   permitted, samples were run at least in duplicate. Precision and accuracy of the squalane

206   internal standard were 2 and <1 ‰, respectively (n=41). Average precision of the n-C_{29} alkane in

207   replicates was 4 ‰. The $\delta^{13}C$ values of the long-chain n-alkanes were measured using a Thermo

208   Trace GC Ultra coupled to a Finnigan MAT 252 isotope ratio monitoring mass spectrometer via a

209   combustion interface operated at 1,000°C. The $\delta^{13}C$ values were calibrated against external CO_2

210   reference gas. $\delta^{13}C$ values are reported in permil (‰) against Vienna Pee Dee Belemnite (VPDB).

211   When concentrations permitted, samples were run at least in duplicate. Precision and accuracy

212   of the squalane internal standard were 0.1 and 0.4 ‰, respectively (n=41). An external standard

213 mixture was analyzed repeatedly every 6 runs and yielded a long-term mean standard deviation

214 of 0.2 ‰ with a mean deviation of 0.1 ‰ from the reference values. Average precision of the n-

215 C_{29} alkane in replicates was 0.3 ‰.

216 2.6 Inorganic geochemistry

217 The elemental composition of all onshore and offshore samples was measured using a

218 combination of high resolution (1 cm) semi-quantitative XRF scanning and lower (5 cm)

219 resolution quantitative XRF measurements on discrete samples (see Suppl. 4). XRF core

220 scanning (Avaatech XRF Scanner II at MARUM, University of Bremen) was performed with an

221 excitation potential of 10 kV, a current of 250 mA, and 30 s counting time for Ca, Fe, K and Al.

222 For discrete measurements on 110 dried and ground samples, a PANalytical Epsilon3-XL XRF

223 spectrometer equipped with a rhodium tube, several filters, and a SSD5 detector was used. A

224 calibration based on certified standard materials (e.g. GBW07309, GBW07316, and MAG-1) was

225 used to quantify elemental counts (c.f. Govin et al., 2012).

226 3 Results and discussion

227 3.1 Proxy indicators

228 3.1.1 SST

229 The magnitude of temperature variability (from ca. 27°C during interglacials to ca. 24°C during

230 glacials) in the GeoB20616-1 Mg/Ca SST record and the timing of changes (postglacial warming

231 at ca. 17 ka BP) correspond to existing regional Mg/Ca SST records (c.f. Fig. 3; Bard et al., 1997;

232 Levi et al., 2007; Wang et al., 2013). They do, however, not correspond to SST calculated from

233 other indicators (i.e. $U^{K'}_{37}$, TEX_{86}) (e.g. Wang et al., 2013; Caley et al., 2011). These indicators

234 show slightly different patterns, which may be attributed to a seasonal bias in the proxies (Wang

235 et al., 2013). Wang et al., (2013) suggest that $U^{K'}_{37}$ SST reflects warm season SST mediated by

236 changes in the Atlantic, whereas the *G. ruber* Mg/Ca SST indicator used in this study records

237 cold season SST mediated by climate changes in the southern hemisphere. This is supported by

238 the youngest SST value (27 °C) at our study site being in agreement with modern Mozambique

239 Channel core-top *G. ruber* SST during austral winter (26°C) rather than austral summer (30°C)

240 (Fallet et al., 2012).

241   3.1.2 Vegetation signatures

242   The major shifts in $\delta^{13}C_{wax}$ values in this record (from ca. -25 ‰ to ca. -24 ‰ at 85 ka BP and

243   from -24 ‰ to − 25 ‰ at ca. 10 ka BP) correspond to vegetation changes detected in the

244   Limpopo catchment just north of our study area (c.f. Fig. 1 a) $\delta^{13}C$ and Fig. 1 c) EM2 (Dupont et

245   al., 2011)). The lighter $\delta^{13}C_{wax}$ values (typical for C_3 woodlands; Magill et al. 2013) during MIS 5

246   and the Holocene in our record correspond to a vegetation described by Dupont et al., (2011) as

247   "woodland and forest in the lowlands and grasslands on the interior plateau" with rivers fringed

248   by "gallery forests" during interglacials. Higher $\delta^{13}C_{wax}$ values typical of C_4 plants (e.g. sedges;

249   Magill et al. 2013) observed in our record during MIS 2, 3 and 4 correspond to a vegetation

250   described as: "open mountain vegetation dominated by ericaceous scrubs with sparse woody

251   vegetation and forest and rivers fringed with open swamps dominated by sedges (Cyperaceae)"

252   during the glacial periods (Dupont et al., 2011; Caley et al., 2018). We focus the discussion on

253   the isotopic signals of the n -C_{31} alkane, as this compound is derived from grasses and trees

254   present throughout the study area. Supplement 3 shows, however, that the n -C_{29} and n -C_{33}

255   alkanes reveal similar trends.

256   3.1.3 Precipitation indicators

257   Hydrogen isotope changes measured in plant waxes are related to the isotope composition of

258   precipitation since hydrogen used for biosynthesis originates directly from the water taken up

259   by the plants (Sessions et al., 1999). In tropical and subtropical areas, the isotopic composition

260   of rainfall (δDp) mainly reflects the amount of precipitation - with δDp depletion indicating

261   more rainfall (Dansgaard, 1964). Furthermore, rainfall D signatures may also become

262   deuterium-depleted with altitude (ca. 10–15 ‰ per 1,000 m, Gonfiantini et al., (2001)). The δD

263   values of leaf waxes in the three catchments are probably affected by both the amount as well

264   as the altitude effect. Rainfall at higher altitudes takes place during times of generally increased

265   rainfall, as it is high precipitation events that reach the interior. The altitude effect therefore

266   enhances the δD depletion of the "amount effect". The K/Al ratio of the sediment is a less direct

267   indicator of the precipitation regime: K/Al has been interpreted as an index between illite

268   (K,H_3O) and kaolinite $(Al_2Si_2O_5(OH)_4)$ giving an indication of the prevailing weathering regime as

269   illite is a product of physical weathering whereas kaolinite is produced during chemical

270   weathering (Clift et al., 2008; Dickson et al., 2010; Burnett et al., 2011). The Ca/Fe ratio is

271   generally used as a proxy of marine (Ca) versus terrestrial (Fe) input to the core site and thus

272   indicative of changes in terrestrial discharge by the river systems (Hebbeln and Cortés, 2001;

273   Croudace et al., 2006; Rogerson et al., 2006; Rothwell and Rack, 2006; McGregor et al., 2009;

274   Dickson et al., 2010; Nizou et al., 2010). The red/blue ratio of the sediment reflects sediment

275   color nuance and increases with sediment lightness. In Geob20616-1 we interpret the reddish

276   values as a more clastic deposition indicative of arid conditions whereas darker blueish colors

277   may reflect clay and organic rich sediments preferentially deposited during humid phases (see

278   also M123 cruise report Zabel, 2006). In the records of δD_{C31}, red/blue , K/Al and Ca/Fe similar

279   patterns can be observed: They all display relatively high values (up to -144 ‰, 1.4; 12 and 0.25

280   respectively) in the intervals marked in red/yellow in Fig.4 and lower values (down to -160, 1.1,

281   1, and 0.2 respectively) in the intervals marked in blue/green in Fig. 4. We associate these

282   variations with (respectively) decreasing (red/yellow) and increasing (blue/green) precipitation

283   over the Incomati, Matola, and Lusutfu catchment areas. The correlation of the four proxies

284   suggests that they may be used as reliable precipitation indicators.

285   3.2 Climatic patterns at different time scales

286   3.2.1 Orbital time scales

287   *3.2.1.1. Sea surface temperatures and vegetation*

288   Over the past 100,000 yrs the SST and $\delta^{13}C_{C31}$ values show a common trend of high SST and low

289    $\delta^{13}C_{wax}$ values during interglacial MIS 5 and 1 and low SST and high $\delta^{13}C$ values during glacial

290   MIS 4-2 (Fig. 3). Our data reveal an increase in SST of ca. 4°C from glacial to interglacial

291   conditions. This correlation between SST and glacial-interglacial changes cycles is commonly

292   found for this area (Caley et al., 2011; Dupont et al., 2011; Caley et al., 2018). On this glacial-

293   interglacial time scale, variations in local SST are thought to be an important driver of

294   hydroclimate in southeastern Africa (c.f. Dupont et al., 2011). During interglacials, warm SST

295   within the Mozambique Channel and Agulhas Current induce an advection of moist air and

296   higher rainfall in the east South African summer rainfall zone (e.g. Walker, 1990; Reason and

297   Mulenga, 1999; Tyson and Preston-Whyte, 2000). The opposite effect is inferred for glacial

298   periods (Dupont et al., 2011; Chevalier and Chase, 2015). The strong influence of western Indian

299   Ocean surface temperatures on the summer precipitation in northern South Africa and

300   southern Mozambique induces a tight coupling between vegetation dynamics in southeastern

301   Africa and sea surface temperature variations in the Western Indian Ocean. This has been

302   shown for several glacial – interglacial cycles in a palynological study offshore Limpopo River

303   (core MD96-2048; Fig. 1) by Dupont et al., (2011). The GeoB20616-1 vegetation indicator

304   ($\delta^{13}C_{wax}$) corresponds to the vegetation shifts that were inferred from the sediments of the

305   Limpopo river (Dupont et al., 2011, Caley et al., 2018). As described in section 3.1.3. these

306   studies reveal a $\delta^{13}C_{wax}$-enriched grassland vegetation for glacial intervals and an increase of

307   woodland vegetation during well-developed interglacial periods, as is the case for MIS 5 and 1

308   (as opposed to MIS 3), reflected in lighter $\delta^{13}C_{wax}$ values. Despite these apparent similarities in

309   the pattern of vegetation shifts detected in the nearby Limpopo river sediment core and at our

310   study site, the mechanisms behind these trends may not be the same. Caley et al., (2018)

311   attribute the $\delta^{13}C_{wax}$-enrichment in Limpopo river sediments during glacials to an expansion of

312   floodplains and the associated C_4 sedges, as well as discharge from the upper Limpopo

313   catchment which reached well into the grassland interior of southern Africa (almost 1,000 km

314   inland). The headwaters of the Incomati, Matola, and Lusutfu catchment areas however are in

315   the Lebombo mountain range located within 200 km of the coast. They do not reach into the

316   interior grassland biomes of South Africa. We therefore propose that in the Incomati, Matola,

317   and Lusutfu catchment areas, the heavier $\delta^{13}C_{wax}$ values for the glacial MIS 4-2 interval reflect

318   retreating forests and an expansion of drought tolerant C_4 plants (grasses) due to growing

319   season aridity, whereas interglacial (MIS 1 and 5) lighter $\delta^{13}C_{wax}$ values reflect the formation of

320   woodlands. Furthermore, sedge-dominated open swamps that fringed rivers during MIS 4-2

321   may have been replaced by gallery forests during MIS1 and 5 (as suggested by Dupont et al.,

322   2011) contributing to the glacial to interglacial $\delta^{13}C_{wax}$ depletion.

323   *3.2.1.2. Hydrology over glacial-interglacial transitions*

324   δD, XRF, and color data are indicators of catchment precipitation changes: decreases in

325   red/blue, Ca/Fe, K/Al ratios and δD values indicate higher precipitation in the catchment, more

326   fluvial discharge and higher chemical weathering rates (see section 3.1.3). Although there is

327   much variability in the hydrological record of core GeoB20616-1, red/blue, Ca/Fe, K/Al ratios

328   and δD values are surprisingly stable over glacial –interglacial transitions (mean δD value of MIS

329   1 and 5: -149 ‰ versus mean δD value of MIS 2-4: -150 ‰). It can be assumed that, during

330   glacials, the rainfall from the main rain bearing systems (SIOCZ related tropical temperate

331   troughs) was reduced due to generally lower land- and sea-surface temperatures and a weaker

332   global hydrological cycle. However, a southward shift of the ITCZ during glacials as previously

333   suggested (Nicholson and Flohn, 1980; Johnson et al., 2002; Chiang et al., 2003; Chiang and

334   Bitz, 2005; Schefuß et al., 2011) would have contributed to increased rainfall in the study area

335   which is nowadays south of direct ITCZ influence. Furthermore, SHW related low pressure

336   systems shifting northward to the Incomati, Matola and Lusutfu catchment areas during glacial

337   conditions may have become a major additional precipitation source. The SHW northward shift

338   of ca. 5° latitude is well documented (Chase and Meadows, 2007; Chevalier and Chase, 2015;

339   Chase et al., 2017; Miller et al., 2019a). The possibility of more frequent SHW related low

340   pressure systems bringing moisture to our study area during the LGM has previous been

341   proposed by Scott et al., (2012) in the framework of a regional pollen review paper. It is also

342   suggested by a modelling study showing an LGM scenario of drier summers and wetter winters

343   for the southeastern African coast (Engelbrecht et al., 2019). During glacial periods, a reduced

344   summer (SIOCZ related) rainfall amount and an increase in SHW related frontal systems as an

345   additional winterly precipitation source, possibly in combination with precipitation from a more

346   southerly ITCZ, would translate to a relatively stable annual rainfall amount over glacial-

347   interglacial transitions.

348   3.2.2 Millennial scale hydrological variability

349   *3.2.2.1 During Interglacial MIS 5*

350   During MIS 5 there are several prominent (ca. -10 ‰) short-term (1-2 ka) decreases in the δD

351   record, which are paralleled with decreases in Ca/Fe, K/Al and red/blue ratios (Fig. 4). We

352   interpret these intervals (approximately 83-80 ka BP and 93-90 ka BP) as wet periods while

353   intervals of high Ca/Fe, K/Al and red/blue ratios and δD values (approximately 97-95 ka BP, 87.5-

354   85 ka BP and 77.5 ka BP) are interpreted as arid intervals (see section 3.1.2. for details on proxy

355   interpretation). During the interglacial MIS 5, millennial scale increases in humidity correlate

356   broadly to periods of warmth in the Antarctic ice core records termed AIM22 and AIM 21 (AIM:

357   Antarctic isotope maxima) (see Fig. 4; EPICA members, 2010). During these Antarctic warm

358   periods, sea ice, the circumpolar circulation and the SHW retracted. This is recorded by

359   Southern Ocean diatom burial rates as well as paleoclimate archives at the southernmost tips of

360   Africa and South America (Lamy et al., 2001; Anderson et al., 2009; Chase et al., 2009; Hahn et

361   al 2016 and references therein; Zhao et al., 2016). It has been hypothesized that southward

362   shifts of the SHW and the South African high-pressure cell, allow the SIOCZ and TTT to shift

363   further south causing an increase in humidity in our study area. Miller et al., (2019b) suggest

364   this mechanism for the region just south of our site (termed *eastern central zone*), which shows

365   Holocene hydroclimatic shifts similar to those recorded in GeoB20616-1. Holocene arid events

366   in this region are attributed to northward shifts of the SHW and the South African high-pressure

367   cell which block the SIOCZ and TTT related moisture. These mechanisms are described in detail

368   by Miller et al., 2019b and our data suggests that they were also active during earlier

369   interglacial periods (e.g. MIS 5) (c.f. schematic model in Fig. 5a). Our current chronology

370   suggests that southward SHW shifts during Antarctic warm periods caused the prominent

371   humid phases during MIS 5 in the Incomati, Matola and Lusutfu catchment areas during the

372   timeframes around 83-80 ka BP (AIM21) and 93-90 ka BP (AIM22). When our best age estimate

373   is applied there is little correspondence between northern or southern insolation maxima and

374   the MIS5 humid phases. In view of the chronological uncertainty in this early part of the record

375   (beyond the C^{14} dating limit), we cannot exclude that these humid phases are related to

376   precessional variability, in the absence of ice interference, causing the division in MIS5a-e.

377   However, in accordance with the conceptual model by Miller et al., (2019b) for the Holocene,

378   we observe no local insolation control on climate at our study site. We suggest that the major

379   shifts in the large-scale rain-bearing systems may override the local insolation forcing.

380   *3.2.2.2. During MIS 4-2 glacial conditions*

381   During the glacial periods MIS 2 and 4 and the less prominent interglacial MIS 3, the correlation

382   between southeastern African humidity and Antarctic warm periods (AIM events) does not

383   persist. In contrast; the first two prominent humid phases in MIS 4 (around 68-63 ka BP and 56

384   ka BP) as well as some of the following more short-term humid phases coincide with cold

385   periods in the Antarctic ice core record (Fig.4). The general position of the SHW trajectories is

386   suggested to have been located 5° in latitude further north during glacial periods (c.f. section

387   *3.2.1.2. Hydrology over glacial-interglacial transitions*). The Incomati, Matola and Lusutfu

388   catchment areas would therefore have been in the direct trajectory of the SHW related low

389   pressure systems. Whilst northward shifts of the SHW and the South African high pressure cell

390   during an interglacial cause aridity by blocking the SIOCZ and TTT (as suggested by Miller et

391   al.,(2019b) and as described in section 3.2.2.1 for e.g. MIS 5), we suggest that during a glacial,

392   additional northward shifts of the SHW (e.g. during Antarctic cold events) would have led to an

393   increase in precipitation related to particularly strong direct influence of the SHW and the

394   related low pressure cells (c.f. schematic model Fig 5b). Fig. 4 also shows a correlation between

395   some of the humid phases during MIS 2-4 and Greenland cold phases i.e. Heinrich stadials. The

396   timing of the wet phases at 68-63 ka, 56 ka, 44 ka, 37 ka, and 23 ka BP corresponds roughly to

397   the following Heinrich stadials: HS6 (after 60 ka BP, Rasmussen et al., 2014); HS5a (56 ka BP,

398   Chapman and Shackleton, 1999); HS5 (45 ka BP; Hemming 2004) and HS4 & HS2 (37 ka BP and

399   23 ka BP, Bond and Lotti, 1995). Wet phases in eastern Africa have previously been associated

400   with Heinrich events (Caley et al., 2018; Dupont et al., 2011; Schefuß et al., 2011). It is well

401   documented that during glacial conditions the large ice masses of the northern hemisphere

402   displace the thermal equator southward (Nicholson and Flohn, 1980; Johnson et al., 2002;

403   Chiang et al., 2003; Chiang and Bitz, 2005; Schefuß et al., 2011). It is therefore hypothesized

404   that the ITCZ reached latitudes further south than its modern maximal extent causing the MIS

405   2-4 rainfall peaks. There is no notable "blocking" effect of the South African high-pressure cell

406   during glacials (schematic model Fig. 5b). The transitions from cold "stadial" to warm

407   "interstadial" conditions and back during MIS 2-4 are extremely rapid and short term. The

408   sampling resolution and age – control of our record (especially prior to ca. 50 ka BP – the limit

409   of C^{14} dating) is not always sufficient for capturing these variations (e.g. HS4). The association of

410   humid phases with a northward shifting SHW and/or southward shifting ITCZ is therefore not

411   always clear and a combination of both may also be possible.

412   *3.2.1.3 From the LGM to the Holocene*

413   Relative to the prolonged arid phase during the late MIS 3/early MIS 2 (37-25 ka BP; c.f. Fig. 4),

414   we observe a trend towards more humid conditions during the LGM (25 – 18 ka BP) marked by a

415   decrease in Ca/Fe, K/Al, red/blue ratios and δD values. This is most likely due to the more

416   frequent SHW-related low-pressure systems bringing moisture to our study area during the LGM

417   and/or southward shifts of the ITCZ as discussed in section *3.2.1.2. Hydrology over glacial-*

418   *interglacial transitions* (see also Fig. 5b). Our record shows a wettening trend after the Last

419   Glacial Maximum and during the deglacial (from ca. 15 ka BP). Several paleoenvironmental

420   records show a common humidity increase for this interval (Meadows 1988; Scott 1989;

421   Norström et al., 2009). Chase et al.,(2017) attribute this to the invigoration of tropical systems

422   with post-glacial warming. The wet conditions prevail until the early Holocene (ca. 8 ka BP).

423   Similar observations of a ca. 15-8 ka BP wet phase have been made in the region (e.g. Norström

424 et al., 2009; Neumann et al., 2010). For this early -Mid Holocene period, we infer from the leaf

425 wax δ^{13}C values a shift from grassland to woodlands as described in section 3.2.1.1. and in

426 Dupont et al. (2011). This may be related to the rainfall intensification as well as to the global

427 temperature and CO_2 increase (c.f. Dupont et al., 2019). The early/Mid Holocene wet phase in

428 our study region (*eastern central SRZ*) is described by Miller et al., 2019b and associated with a

429 southward shift of the SHW and the South African high-pressure cell allowing for the SIOCZ

430 related rain bearing systems (TTT) to shift southward over the region. The late Holocene (the

431 last 5 kyrs) however, was an arid phase at our study cite as suggested by the precipitation

432 indicators δD, Ca/Fe, K/Al and red/blue ratios. Several regional records (e.g. Mfabeni peatlands

433 and the *eastern-central region*) show similar shifts; from a wet deglacial / Early Holocene (18-5

434 ka BP) to dry conditions thereafter (Chevalier et al., 2015; Miller et al., 2019a). Miller et al.

435 (2019b) compile eastern African climate records and recognize a late Holocene tripole of

436 increased humidity north of 20°S and south of 25°S and a contrasting aridity trend in the region

437 in-between. Our catchment is located at the northernmost extent of this intermediate region;

438 while we record an aridity trend in the Late Holocene, the adjacent Limpopo catchment just to

439 the north received higher rainfall amounts during this time interval (Miller et al., 2019b). A

440 northward shift in SHW with the South African high-pressure cell blocking the SIOCZ and TTT is

441 a suggested mechanism for this late Holocene aridity (Miller et al., 2019b; also described in

442 section 3.2.2.1). Likewise, Mason and Jury (1997) (based on a conceptual model by Tyson

443 (1984)) suggest that northward shifting SHW induce rain-bearing low pressure cells to shift

444 away from the eastern African coast towards Madagascar. During the Late Holocene the modern

445 climatic situation of the study area was established: during the summer months the SHW and

446 the South African high-pressure cell are in their southernmost position allowing the SIOCZ

447 related TTT to bring rainfall to the region (66 % of annual precipitation). During the winter

448 months the SHW and the South African high-pressure cell shift northward. In this constellation

449 the SIOCZ and TTT influence are blocked by the South African high-pressure cell, however low-

450 pressure cells may become cut from the main SHW flow bringing winterly rainfall to the area (33

451 % of annual precipitation) as described in section 1.2.

452 Conclusions

453 Using the organic and inorganic geochemical properties of sediment core GeoB20616-1 from

454 the Delagoa Bight we were able to reconstruct the vegetation changes and rainfall patterns in

455 the Incomati, Matola and Lusutfu catchments as well as SST trends of the Agulhas waters for the

456 past ca. 100,000 yrs offshore southeastern Africa. Our reconstructions underline the existing

457 dipoles or tripoles in southeastern African climate: although the glacial-interglacial variability at

458 our site resembles that observed in the adjacent Limpopo river catchment, the Holocene

459 hydrological trends are exactly inverted in these neighboring catchments. Small-scale climatic

460 zones have been previously described for the region (c.f. Scott et al., 2012; Chevalier and Chase,

461 2015; Miller et al., 2019b) and each zone has been attributed to a climatic driving mechanism.

462 Our data provide insights into the spatial shifts of these zones as fundamental shifts in the

463 major climate systems occurred over glacial-interglacial cycles. In accordance with Miller et al.,

464 (2019b) we identify displacements of the SHW as the main hydro-climate driver during the

465 Holocene in our study area (termed *central and eastern zone*). The main trajectories of the SHW

466 related disturbances remain so far south during the Holocene, that they rarely deliver direct

467 rainfall to the study area. Instead, northward shifts of the SHW and the South African high-

468 pressure cell block the SIOCZ and thus TTT related rainfalls over the region (Fig. 5a). In this

469 manner latitudinal SHW shifts influence the local rainfall indirectly. Our study not only confirms

470 the Miller et al. (2019 b) conceptual model for the Holocene, but also finds the same

471 mechanisms to be active during MIS5. As Miller et al. (2019b) we find an absence of insolation

472 forcing in our study area. We suggest that at these latitudes local insolation as a climatic forcing

473 mechanism is overridden by shifts in the major rain-bearing systems. We conclude that during

474 interglacials regional wet phases are induced by southward shifting westerlies (related to

475 Antarctic warming trends) allowing for the influence of the SIOCZ related TTT. During glacial

476 periods, however, we observe an inverted relationship between Antarctic warm events and

477 regional humidity, and an additional correlation of several humid intervals with extreme

478 northern hemispheric cold events (HS). This suggests that the mechanisms driving the millennial

479 scale hydrological variability during glacials are not the same as during interglacials. We

480 attribute this to the global reorganization of climate systems during the glacial as the large ice

481 masses at both poles induce a southward shift of the thermal equator and the ITCZ as well as a

482 northward shift of the SHW. Our study site is located at the interface of these "compressed"

483 climate systems. As a result, during full glacial conditions, the region may have received

484 precipitation both from SHW related disturbances as well as from SIOCZ related TTT (Fig. 5b). In

485 this "compressed" state the northward shifts of the SHW and the South African high pressure

486 no longer have the net effect of blocking SIOCZ related precipitation; as this is compensated by

487   the increase in winterly rains. Overall humidity therefore shows no considerable decrease

488   during MIS 2-4. Nevertheless, a shift in vegetation from woodland to grasslands takes place

489   during glacials; we attribute this to a reduced growing-season (summer) precipitation, probably

490   in combination with low temperatures and atmospheric CO_2. Our study shows that these

491   mechanisms are active in a spatially very restrained area resulting in small-scale variability.

492   These small-scale climatic dipoles or tripoles make the southeastern African coastal area

493   especially sensitive to shifts in the global climatic system.

506   Contributor Roles

507   Annette Hahn: conceptualization, investigation, analysis, visualisation, writing

508   Enno Schefuß: funding acquisition, conceptualization, investigation, review & editing

509   Jeroen Groeneveld: analysis, interpretation, methodology, review & editing

510   Charlotte Miller: analysis, interpretation, review & editing

511   Matthias Zabel: funding acquisition, project administration, conceptualization, investigation,

512   review & editing

513   Sample and data availability

514   Samples and data are respectively archived at the GeoB Core Repository and Pangaea

515   (www.pangaea.de) both located at MARUM, University of Bremen.

References

Anderson, R. F., Ali, S., Bradtmiller, L. I., Nielsen, S. H. H., Fleisher, M. Q., Anderson, B. E., and Burckle, L. H.: Wind-Driven Upwelling in the Southern Ocean and the Deglacial Rise in Atmospheric CO_2, Science, 323, 1443-1448, https:doi.org/10.1126/science.1167441, 2009.

Baker, A., Pedentchouk, N., Routh, J., Roychoudhury, A. N.: Climatic variability in peatlands (South Africa) since the late Pleistocene, Quat. Sci. Rev. , 160: 57-66, 2017.

Baray, J. L., Baldy, S., Diab, R. D., Cammas, J. P.: Dynamical study of a tropical cut-off low over South Africa, and its impact on tropospheric ozone, Atmos. Environ., 37(11), 1475-1488, 2003.

Bard, E., Rostek, F., Sonzogni, C.: Interhemispheric synchrony of the last deglaciation inferred from alkenone palaeothermometry, Nature, 385(6618), 707, 1997.

Barker, S., Greaves, M., and Elderfield, H.: A study of cleaning procedures used for foraminiferal Mg/Ca paleothermometry, Geochemistry, Geophysics, Geosystems, 4, 10.1029/2003gc000559, 2003.

Biastoch, A., Reason, C. J. C., Lutjeharms, J. R. E., Boebel, O.: The importance of flow in the Mozambique Channel to seasonality in the greater Agulhas Current system, Geophys. Res. Lett., 26, 3321-3324, 1999.

Blaauw, M., Christen, J. A.: Flexible paleoclimate age-depth models using an autoregressive gamma process, Bayesian analysis, 6(3), 457-474, 2011.

Bond, G. C. and Lotti, R.: Iceberg Discharges into the North Atlantic on Millennial Time Scales During the Last Glaciation, Science 267(5200), 1005-1010, 1995.

Burnett, A. P., Soreghan, M. J., Scholz, C. A., Brown, E. T.: Tropical East African climate change and its relation to global climate: a record from Lake Tanganyika, Tropical East Africa, over the past 90+ kyr, Palaeogeogr. Palaeoclimatol. Palaeoecol., 303(1-4), 155-167, 2011.

Caley, T., Extier, T., Collins, J. A., Schefuß, E., Dupont, L., Malaizé, B., Rossignol, L., Souron, A., McClymont, E. L., and Jimenez-Espejo, F. J.: A two-million-year-long hydroclimatic context for hominin evolution in southeastern Africa, Nature, 1, 2018.

Caley, T., Malaizé, B., Revel, M., Ducassou, E., Wainer, K., Ibrahim, M., Shoeaib, D., Migeon, S., and Marieu, V.: Orbital timing of the Indian, East Asian and African boreal monsoons and the concept of a 'global monsoon', Quat. Sci. Rev., 30, 3705-3715, 2011.

Chapman, M. R. and Shackleton N. J.: Global ice-volume fluctuations, North Atlantic ice-rafting events, and deep-ocean circulation changes between 130 and 70 ka, Geology, 27(9), 795-798, 1999.

Chase, B. M., Chevalier, M., Boom, A., Carr, A. S.: The dynamic relationship between temperate and tropical circulation systems across South Africa since the last glacial maximum, Quat. Sci. Rev., 174, 54-62, 2017.

Chase, B. M., Faith, J. T., Mackay, A., Chevalier, M., Carr, A. S., Boom, A., Lim, S., and Reimer, P. J.: Climatic controls on Later Stone Age human adaptation in Africa's southern Cape, J. Hum. Evol., 114, 35-44, 2018.

Chase, B. M., Meadows, M. E.: Late Quaternary dynamics of southern Africa's winter rainfall zone, Earth Sci. Rev., 84(3-4), 103-138, 2007.

Chase, B., Meadows, M., Scott, L., Thomas, D., Marais, E., Sealy, J., and Reimer, P.: A record of rapid Holocene climate change preserved in hyrax middens from southwestern Africa, Geology, 37, 703-706, 2009.

Chevalier, M., Brewer, S., Chase, B. M.: Qualitative assessment of PMIP3 rainfall simulations across the eastern African monsoon domains during the mid-Holocene and the Last Glacial Maximum, Quat. Sci. Rev., 156, 107-120, 2017.

Chevalier, M., Chase, B. M.: Southeast African records reveal a coherent shift from high- to low-latitude forcing mechanisms along the east African margin across last glacial–interglacial transition, Quat. Sci. Rev., 125, 117-130, 2015.

Chiang, J. C. H., Biasutti, M., Battisti, D. S.: Sensitivity of the Atlantic Intertropical Convergence Zone to Last Glacial Maximum boundary conditions, Paleoceanogr., 18(4), 2003.

Chiang, J. C. H., Bitz, C. M.: Influence of high latitude ice cover on the marine Intertropical Convergence Zone, Clim. Dyn., 25(5), 477-496, 2005.

Clift, P. D., Hodges, K. V., Heslop, D., Hannigan, R., Van Long, H., and Calves, G.: Correlation of Himalayan exhumation rates and Asian monsoon intensity, Nat. Geosci., 1, 875, 2008.

Croudace, I. W., Rindby, A., Rothwell, R. G.: ITRAX: Description and evaluation of a new multi-function X-ray core scanner, Geol. Soc. Spec. Publ., London, 267(1), 51-63, 2006.

Dansgaard, W.: Stable isotopes in precipitation, Tellus, 16(4), 436-468, 1964.

De Wit, M. J., De Ronde, C. E. J., Tredoux, M., Roering, C., Hart, R. J., Armstrong, R. A., Green, R. W. E., Peberdy, E., and Hart, R. A.: Formation of an Archaean continent, Nature, 357, 553-562, https:doi.org /10.1038/357553a0, 1992.

Dickson, A., Leng, M., Maslin, M., Röhl, U.: Oceanic, atmospheric and ice-sheet forcing of Southeast Atlantic Ocean productivity and South African monsoon intensity during MIS-12 to 10, Quat. Sci. Rev., 29, 3936-3947, 2010.

Dupont, L. M., Caley, T., Kim, J. H., Castañeda, I., Malaizé, B., and Giraudeau, J.: Glacial-interglacial vegetation dynamics in Southeastern Africa coupled to sea surface temperature variations in the Western Indian Ocean, Clim. Past, 7, 1209-1224, https:doi.org /10.5194/cp-7-1209-2011, 2011.

Dupont, L. M., Caley, T., and Castañeda, I. S.: Effects of atmospheric CO_2 variability of the past 800kyr on the biomes of southeast Africa, Clim. Past, 15, 1083-1097, 10.5194/cp-15-1083-2019, 2019.

Eglinton, G., and Hamilton, R. J.: Leaf epicuticular waxes, Science, 156, 1322-1335, 1967.

Engelbrecht, F. A., Marean, C. W., Cowling, R. M., Engelbrecht, C. J., Neumann, F. H., Scott, L., Nkoana, R., O'Neal, D., Fisher, E., Shook, E., Franklin, J., Thatcher, M., McGregor, J. L., Van der Merwe, J., Dedekind, Z., and Difford, M.: Downscaling Last Glacial Maximum climate over southern Africa, Quaternary Science Reviews, 226, 105879, https://doi.org/10.1016/j.quascirev.2019.105879, 2019.

EPICA Members: Stable oxygen isotopes of ice core EDML, PANGAEA, 2010

Fallet, U., Castañeda, I. S., Henry-Edwards, A., Richter, T. O., Boer, W., Schouten, S., and Brummer, G.-J.: Sedimentation and burial of organic and inorganic temperature proxies in the Mozambique Channel, SW Indian Ocean, Deep Sea Research Part I, Oceanographic Research Papers, 59, 37-53, 2012.

Gasse, F., Chalié, F., Vincens, A., Williams M. A. J., and Williamson D.: Climatic patterns in equatorial and southern Africa from 30,000 to 10,000 years ago reconstructed from terrestrial and near-shore proxy data, Quat. Sci. Rev., 27(25), 2316-2340, 2008.

Gonfiantini, R., Roche, M.-A., Olivry, J.-C., Fontes, J.-C., Zuppi, G. M.: The altitude effect on the isotopic composition of tropical rains, Chem. Geol., 181(1–4), 147-167, 2001.

Govin, A., Holzwarth, U., Heslop, D., Ford Keeling, L., Zabel, M., Mulitza, S., Collins, J. A., and Chiessi, C. M.: Distribution of major elements in Atlantic surface sediments (36°N–49°S): Imprint of terrigenous input and continental weathering, Geochem. Geophys. Geosys., 13, https:doi.org /Q01013, 10.1029/2011GC003785, 2012.

Climate
of the Past
Discussions

Greaves, M., Caillon, N., Rebaubier, H., Bartoli, G., Bohaty, S., Cacho, I., Clarke, L., Cooper, M., Daunt, C., and Delaney, M.: Interlaboratory comparison study of calibration standards for foraminiferal Mg/Ca thermometry, Geochem. Geophys. Geosys., 9, 2008.

Groeneveld, J., Filipsson, H.: Mg/Ca and Mn/Ca ratios in benthic foraminifera: the potential to reconstruct past variations in temperature and hypoxia in shelf regions, Biogeosci., 10(7), 5125-5138, 2013.

Hahn, A., Schefuß, E., Andò, S., Cawthra, H. C., Frenzel, P., Kugel, M., Meschner, S., Mollenhauer, G., and Zabel, M.: Linking catchment hydrology and ocean circulation in Late Holocene southernmost Africa, Climate of the Past Discussions. doi, 10, 2016.Hebbeln, D., Cortés, J.: Sedimentation in a tropical fjord: Golfo Dulce, Costa Rica, Geo-Marine Letters, 20(3), 142-148, 2001.

Hemming, S. R.: Heinrich events: Massive late Pleistocene detritus layers of the North Atlantic and their global climate imprint, Rev. Geophys., 42, https:doi.org /10.1029/2003RG000128, 2004.

Johnson, T. C., Brown, E. T., McManus, J., Barry, S., Barker, P., and Gasse, F.: A high-resolution paleoclimate record spanning the past 25,000 years in southern East Africa, Science, 296, 113-132, https:doi.org /10.1126/science.1070057, 2002.

Jury, M. R., Valentine, H. R., Lutjeharms, J. R. E.: Influence of the Agulhas Current on Summer Rainfall along the Southeast Coast of South Africa, J. Appl. Meteorol., 32(7), 1282-1287, 1993.

Kersberg, H.: Vegetationsgeographie, Südafrika (Mosambik, Swasiland, Republik Südafrika), Gebrüder Borntraeger, 1996.

Lamy, F., Hebbeln, D., Röhl, U., and Wefer, G.: Holocene rainfall variability in southern Chile: a marine record of latitudinal shifts of the Southern Westerlies, Earth and Planetary Science Letters, 185, 369-382, 2001.

Lea, D. W., Pak, D. K., Peterson, L. C., and Hughen, K. A.: Synchroneity of tropical and high-latitude Atlantic temperatures over the last glacial termination, science, 301, 1361-1364, 2003.

Levi, C., Labeyrie, L., Bassinot, F., Guichard, F., Cortijo, E., Waelbroeck, C., Caillon, N., Duprat, J., de Garidel-Thoron, T., and Elderfield, H.: Low-latitude hydrological cycle and rapid climate changes during the last deglaciation, Geochem. Geophys. Geosyst., 8, 2007.

Lisiecki, L. E., Raymo, M. E.: A Pliocene-Pleistocene stack of 57 globally distributed benthic δ^{18}O records, Paleoceanogr., 20(1), 2005.

Locarnini, R. A., Mishonov, A. V., Antonov, J. I., Boyer, T. P., Garcia, H. E., Baranova, O. K., Zweng, M. M., Paver, C. R., Reagan, J. R., Johnson, D. R., Hamilton, M., Seidov, D., and Levitus, S.: World ocean atlas 2013, Volume 1, Temperature, http://doi.org/10.7289/V55X26VD, 2013.

Lutjeharms, J. R. E., and Da Silva, A. J., 1988, The Delagoa Bight eddy: Deep Sea Research Part A.

Magill, C.R., Ashley, G.M., Freeman, K.H., 2013. Ecosystem variability and early human habitats in eastern Africa. Proceedings of the National Academy of Sciences 110, 1167-1174. Oceanographic Research Papers, v. 35, p. 619-634.

Maboya, L., Meadows, M., Reimer, P., Haberzettl, T.: Marine reservoir correction ΔAR, for south and east coasts of South Africa, 21st Biennial Conference of the South African Society of Quaternary Research, Johannesburg, 3–7 April 2017, 25, 2017.

Mason, S., Jury, M.: Climatic variability and change over southern Africa: a reflection on underlying processes, Prog. Phys. Geogr., 21(1), 23-50, 1997.

McGregor, H. V., Dupont, L., Stuut, J.-B. W., Kuhlmann, H.: Vegetation change, goats, and religion: a 2,000-year history of land use in southern Morocco, Quat. Sci. Rev., 28(15), 1434-1448, 2009.

Miller, C., Finch, J., Hill, T., Peterse, F., Humphries, M., Zabel, M., and Schefuß, E.: Late Quaternary climate variability at Mfabeni peatland, eastern South Africa, Clim. Past, 15, 1153-1170, https:doi.org /10.5194/cp-15-1153-2019, 2019.

Miller, C., Hahn, A., Zabel, M., Schefuß, E.: Mid- and low latitude effects on eastern South African rainfall over the last 7 thousand years , Quat. Sci. Rev., 2019.

Neumann, F. H., Scott, L., Bousman, C. B., and Van As, L.: A Holocene sequence of vegetation change at Lake Eteza, coastal KwaZulu-Natal, South Africa, Rev. Palaeobot. Palynol., 162, 39-53, https://doi.org/10.1016/j.revpalbo.2010.05.001, 2010.

NGRIP members,: High-resolution record of Northern Hemisphere climate extending into the last interglacial period, Nature 431(7005), 147-151, 2004.

Nicholson, S. E., Flohn, H.: African environmental and climatic changes and the general atmospheric circulation in late Pleistocene and Holocene, Clim. Change, 2(4), 313-348, 1980.

Climate
of the Past
Discussions

Nizou, J., Hanebuth, T. J. J., and Vogt, C.: Deciphering signals of late Holocene fluvial and aeolian supply from a shelf sediment depocenter off Senegal (north-west Africa), J. Quat. Sci., 26, 411-421, https:doi.org /10.1002/jqs.1467, 2010.

Norström, E., Scott, L., Partridge, T., Risberg, J., and Holmgren, K.: Reconstruction of environmental and climate changes at Braamhoek wetland, eastern escarpment South Africa, during the last 16,000 years with emphasis on the Pleistocene–Holocene transition, Palaeogeogr. Palaeoclimatol. Palaeoecol., 271, 240-258, 2009.

Paillard, D., Labeyrie, L., and Yiou, P.: Macintosh program performs time‐series analysis, Eos, Transactions American Geophysical Union, 77, 379-379, 1996.

Partridge, T. C., Demenocal, P. B., Lorentz, S. A., Paiker, M. J., Vogel, J. C.: Orbital forcing of climate over South Africa: A 200,000-year rainfall record from the pretoria saltpan, Quat. Sci. Rev., 16(10), 1125-1133, 1997.

Quartly, G. D., and Srokosz, M. A., 2004, Eddies in the southern Mozambique Channel: Deep Sea Research Part II: Topical Studies in Oceanography, v. 51, p. 69-83.Rasmussen, S. O., Bigler, M., Blockley, S. P., Blunier, T., Buchardt, S. L., Clausen, H. B., Cvijanovic, I., Dahl-Jensen, D., Johnsen, S. J., Fischer, H., Gkinis, V., Guillevic, M., Hoek, W. Z., Lowe, J. J., Pedro, J. B., Popp, T., Seierstad, I. K., Steffensen, J. P., Svensson, A. M., Vallelonga, P., Vinther, B. M., Walker, M. J. C., Wheatley, J. J., and Winstrup, M.: A stratigraphic framework for abrupt climatic changes during the Last Glacial period based on three synchronized Greenland ice-core records: refining and extending the INTIMATE event stratigraphy, Quat. Sci. Rev., 106, 14-28, https://doi.org/10.1016/j.quascirev.2014.09.007, 2014.

Reason, C., Mulenga, H.: Relationships between South African rainfall and SST anomalies in the southwest Indian Ocean, Int. J. Climatol., 19, 1651-1673, 1999.

Reason, C., Rouault, M.: Links between the Antarctic Oscillation and winter rainfall over western South Africa, Geophys. Res. Lett., 32(7), 2005.

Reimer, P. J., Bard, E., Bayliss, A., Beck, J. W., Blackwell, P. G., Ramsey, C. B., Buck, C. E., Cheng, H., Edwards, R. L., and Friedrich, M.: IntCal13 and Marine13 radiocarbon age calibration curves 0–50,000 years cal BP, Radiocarbon, 55, 1869-1887, 2013.

Rogerson, M., Rohling, E., Weaver, P.: Promotion of meridional overturning by Mediterranean-derived salt during the last deglaciation, Paleoceanogr., 21(4), 2006.

Rothwell, R. G., Rack, F. R.: New techniques in sediment core analysis: an introduction, Geol. Soc. Spec. Publ., 267(1), 1-29, https://doi.org/10.1144/GSL.SP.2006.267.01.01, 2006.

Climate
of the Past
Discussions

Schefuß, E., Kuhlmann, H., Mollenhauer, G., Prange, M., Patzold, J.: Forcing of wet phases in southeast Africa over the past 17,000 years, Nature, 480(7378), 509-12, 2011.

Schüürman, J., Hahn, A., Zabel, M.: In search of sediment deposits from the Limpopo (Delagoa Bight, southern Africa): Deciphering the catchment provenance of coastal sediments, Sediment. Geol., 380, 94-104, 2019.

Scott, L., Neumann, F. H., Brook, G. A., Bousman, C. B., Norström, E., and Metwally, A. A.: Terrestrial fossil-pollen evidence of climate change during the last 26 thousand years in Southern Africa, Quat. Sci. Rev., 32, 100-118, https:doi.org/10.1016/j.quascirev.2011.11.010, 2012.

Sessions, A. L., Burgoyne, T. W., Schimmelmann, A., Hayes, J. M.: Fractionation of hydrogen isotopes in lipid biosynthesis, Org. Geochem., 30(9), 1193-1200, 1999.

Sigman, D. M., Hain, M. P., Haug, G. H.: The polar ocean and glacial cycles in atmospheric CO_2 concentration, Nature, 466, 47, 2010.

Simon, M. H., Ziegler, M., Bosmans, J., Barker, S., Reason, C. J. C., and Hall, I. R.: Eastern South African hydroclimate over the past 270,000 years, Sci. Rep., 5, 18153, https:doi.org /10.1038/srep18153, 2015.

Sonzogni, C., Bard, E., and Rostek, F.: Tropical sea-surface temperatures during the last glacial period: a view based on alkenones in Indian Ocean sediments, Quaternary Science Reviews, 17, 1185-1201, 1998.

Stager, J. C., Mayewski, P. A., White, J., Chase, B. M., Neumann, F. H., Meadows, M. E., King, C. D., and Dixon, D. A.: Precipitation variability in the winter rainfall zone of South Africa during the last 1400 yr linked to the austral westerlies, Climate of the Past Discussions, 7, 4375-4399, https:doi.org /10.5194/cpd-7-4375-2011, 2011.

Stuiver, M., Reimer, P., Reimer, R.: CALIB 7.1, http://calib.org, accessed 2019-8-23, 2019.

Sweeney, R. J., Duncan, A. R., Erlank, A. J.: Geochemistry and Petrogenesis of Central Lebombo Basalts of the Karoo Igneous Province, J. Petrol., 35(1), 95-125, 1994.

Tierney, J. E., Russell, J. M., Huang, Y., Damsté, J. S. S., Hopmans, E. C., and Cohen, A. S.: Northern Hemisphere Controls on Tropical Southeast African Climate During the Past 60,000 Years, Science, 322, 252-255, https:doi.org /10.1126/science.1160485, 2008.

Truc, L., Chevalier, M., Favier, C., Cheddadi, R., Meadows, M. E., Scott, L., Carr, A. S., Smith, G. F., and Chase, B. M.: Quantification of climate change for the last 20,000years from Wonderkrater, South Africa: Implications for the long-term dynamics of the Intertropical

Convergence Zone, Palaeogeogr. Palaeoclimatol. Palaeoecol., 386, 575-587, https://doi.org/10.1016/j.palaeo.2013.06.024, 2013.

Tyson, P. D., Preston-Whyte, R. A.: Weather and climate of southern Africa, Oxford University Press., 2000.

Tyson, P. D.: The atmospheric modulation of extended wet and dry spells over South Africa, 1958–1978, Int. J. Climatol., 4, 621-635, https:doi.org /10.1002/joc.3370040606, 1984.

Walker, N. D.: Links between South African summer rainfall and temperature variability of the Agulhas and Benguela Current systems, J. Geophys. Res., 95(C3), 3297-3319, 1990.

Wang, Y. V., Leduc, G., Regenberg, M., Andersen, N., Larsen, T., Blanz, T., and Schneider, R. R.: Northern and southern hemisphere controls on seasonal sea surface temperatures in the Indian Ocean during the last deglaciation, Paleoceanogr., 28, 619-632, https:doi.org /10.1002/palo.20053, 2013.

White, F.,: The vegetation of Africa, Natural Resources Research, 20 UNESCO, Paris, 1983.

Xie, P., and Arkin, P. A.: Global precipitation: A 17-year monthly analysis based on gauge observations, satellite estimates, and numerical model outputs, Bull. Am. Meteorol. Soc., 78, 2539-2558, 1997.

Zabel, M.: Climate archives in coastal waters of southern Africa–Cruise No. M123–February 3–February 27, 2016–Walvis Bay (Namibia)–Cape Town (Rep. of South Africa), METEOR-Berichte M 123, 50, 2016.

Zhao, X., Dupont, L., Schefuß, E., Meadows, M., Hahn, A., and Wefer, G.: Holocene vegetation and climate variability between winter and summer rainfall zones of South Africa, Quat. Int., 404, 185-186, 2016.

Zahn, R., Hall, I., Schneider, R., Barker S., Compton, J., Dupont, L., Flores, J.-A., Franzese, A., Goldstein,S., Hemming, S., Knorr, G., Marino, G., Mazaud, A., Peeters, F., Preu, B., Reichert, G.-J., Spiess, V., Uenzelmann-Neben, G., Weldcab, S., Ziegler, M., 2012, Southern African Climates, Agulhas Warm Water Transports and Retroflection, and Interocean Exchanges - SAFARI: International Ocean Discovery Program.

Ziegler, M., Simon, M. H., Hall, I. R., Barker, S., Stringer, C., and Zahn, R.: Development of Middle
Stone Age innovation linked to rapid climate change, Nat. Commun., 4, 1905, https:doi.org
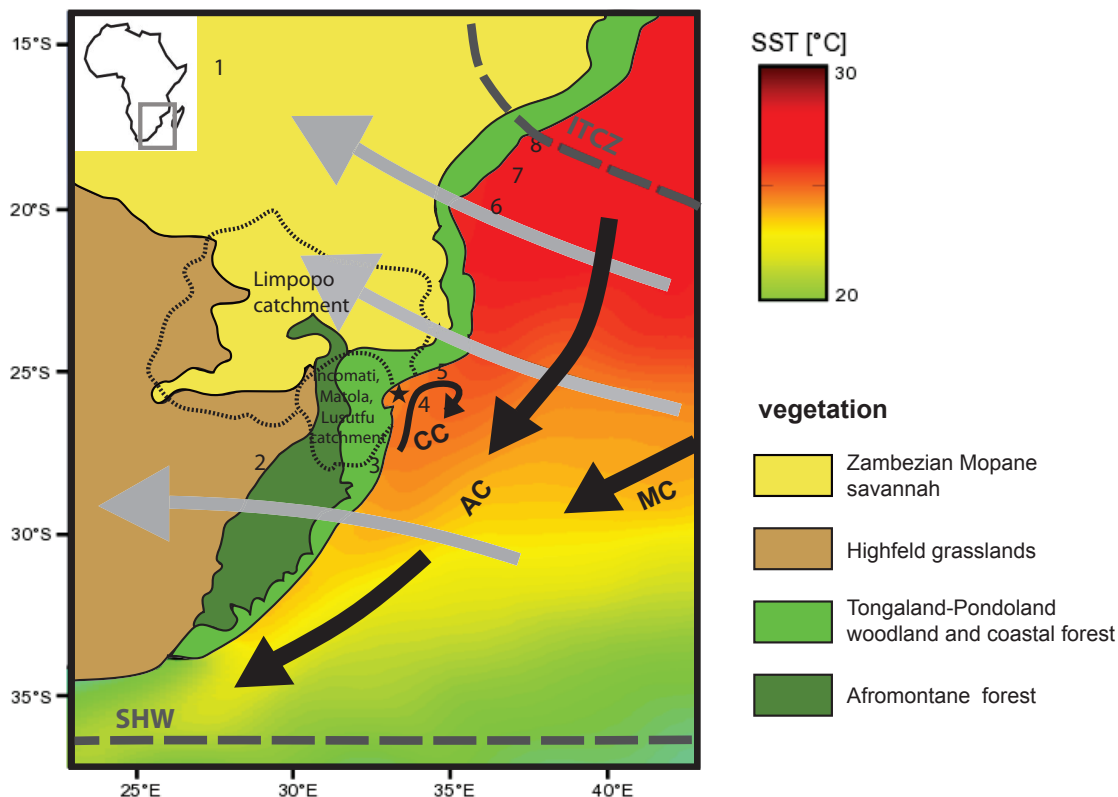/10.1038/ncomms2897, 2013.

Fig. 1 Modern vegetation of southern Africa and the Incomati, Matola and Lusutfu catchments (after White 1983) and annual SST over the Indian Ocean (Locarnini et al., 2013). Grey arrows represent the atmospheric circulation over southern Africa during austral summer. The approximate modern summer position of the ITCZ (intertropical convergence zone) and modern winter position of the SHW (southern hemispheric westerlies) is indicated. Mozambique current (MC), Agulhas current (AC), and counter current (cc) forming a coastal eddy are shown. GeoB20616-1 is marked by a star. Sites mentioned in the discussion are numbered as: 1) Wonderkrater (Truc et al., 2013); 2) Braamhoek (Norström et al., 2009); 3) Mfabeni (Miller et al., 2019a); 4) MD96-2048 (Dupont et al., 2011; Caley et al., 2011, 2018); 5) GeoB20610-1 (Miller et al., 2019b); 6) GIK16160-3 (Wang et al., 2013); 7) MD79-257 (Bard et al., 1997; Sonzogni et al., 1998; Levi et al., 2007); 8) GeoB9307-3 (Schefuß et al., 2011).
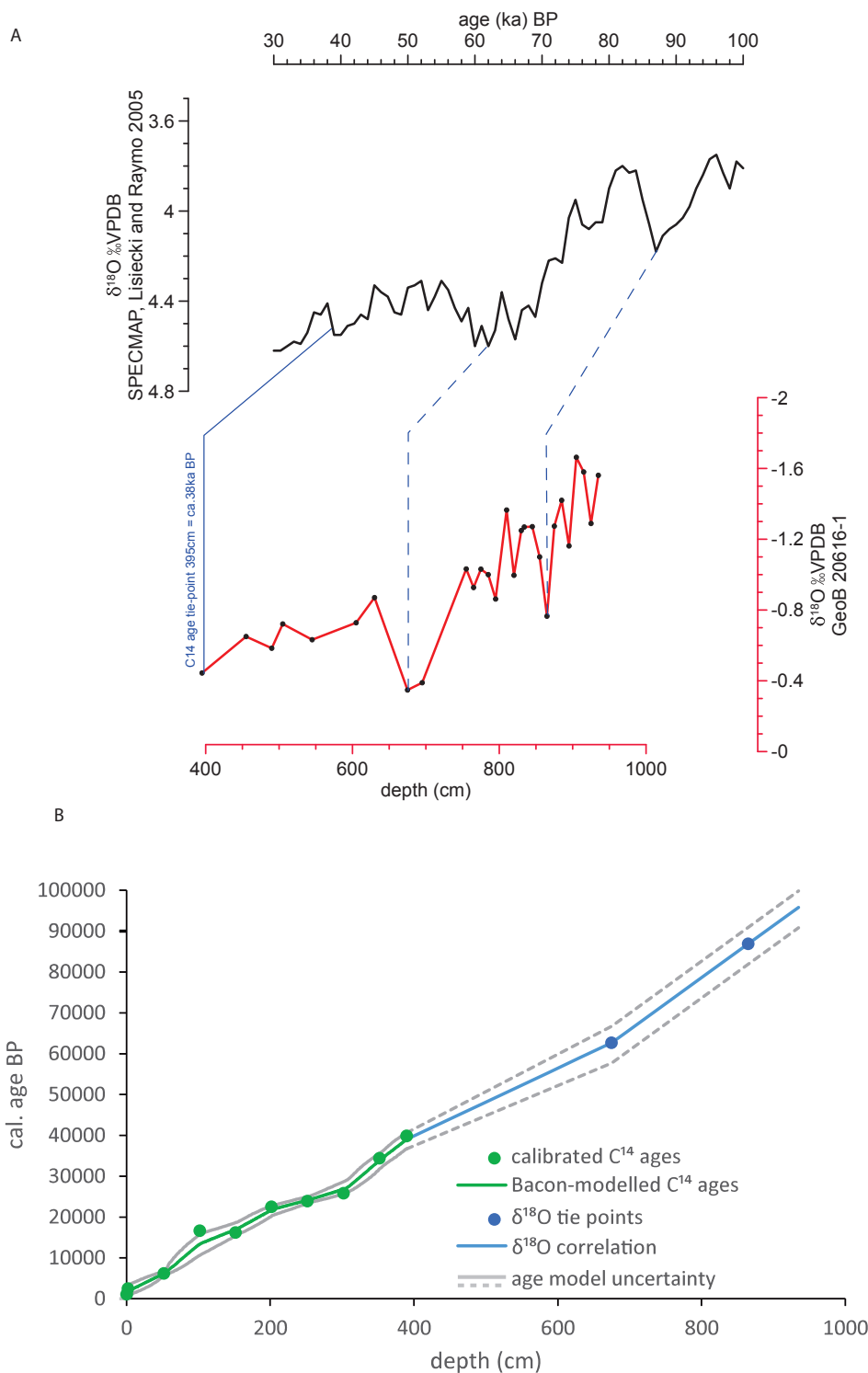
Fig. 2 Reference curves and age–depth model of core GeoB20616-1. A: LR04 benthic foraminifera δ^{18}O stack LR04 (Lisiecki and Raymo, 2005) (black) compared to GeoB20616-1 (red) *G. ruber* foraminifera δ^{18}O with indicated tie points. B: Age-depth model based on Bacon v. 2.2 (Blaauw and Christen, 2011; green) and δ^{18}O correlation (blue). Blue circles in panel B represent the positions of calibrated ^{14}C ages whereas blue circles indicate δ^{18}O tie points. Grey lines indicate uncertainty.
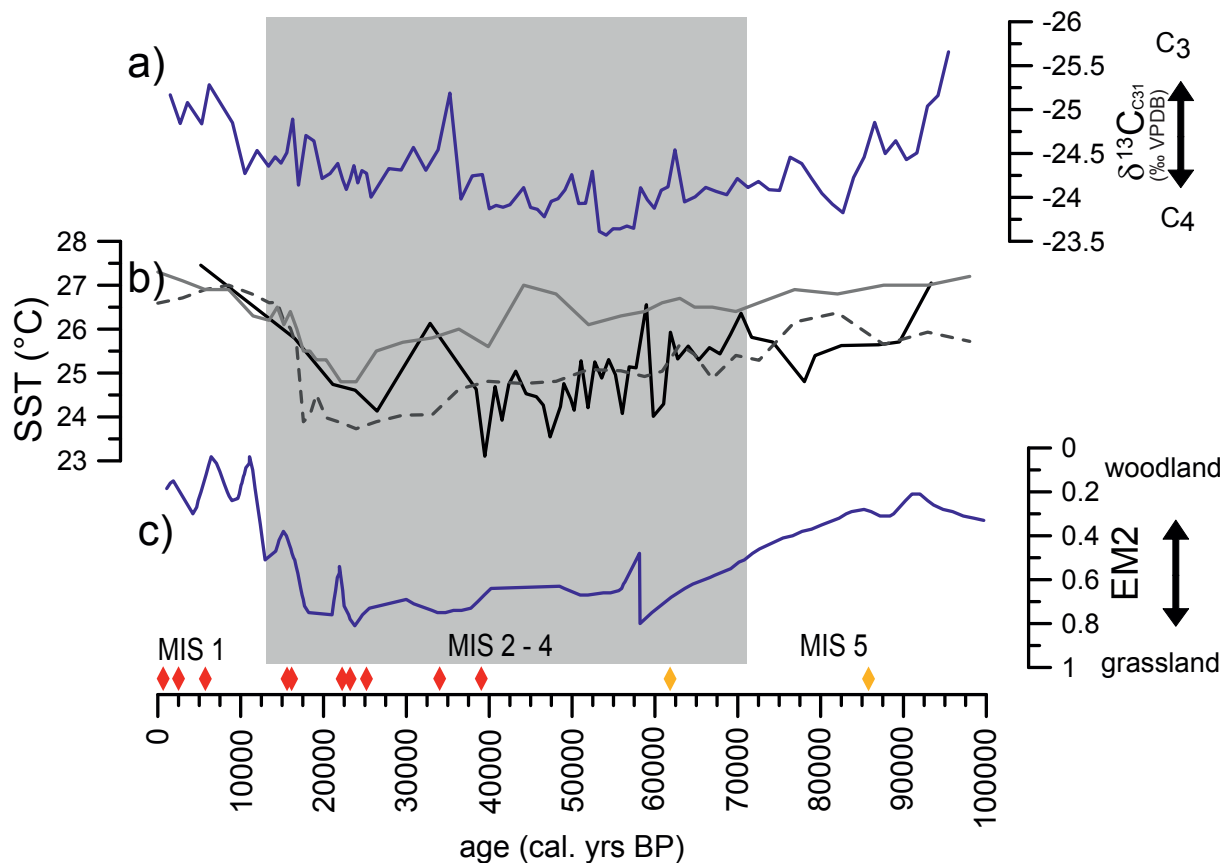
Fig. 3 Down-core δ^{13}C values of the C$_{31}$ n- alkane in ‰ VPDB of GeoB20616-1 as indicators for shifts in vegetation type (a): C$_4$ vs. C$_3$) as well as SST recorded by *G. ruber* Mg/Ca (b): black line). For comparative purposes the following data is also shown: b): offshore (MD96-2048) Limpopo River SST calculated from TEX$_{86}$ (dashed line) and from U$^{K'}_{37}$ (grey line) from Caley et al., (2011) and c): Limpopo vegetation endmember EM2 from Dupont et al., (2011). The diamonds indicate C^{14} dates (red) and δ^{18}O tie points (orange).
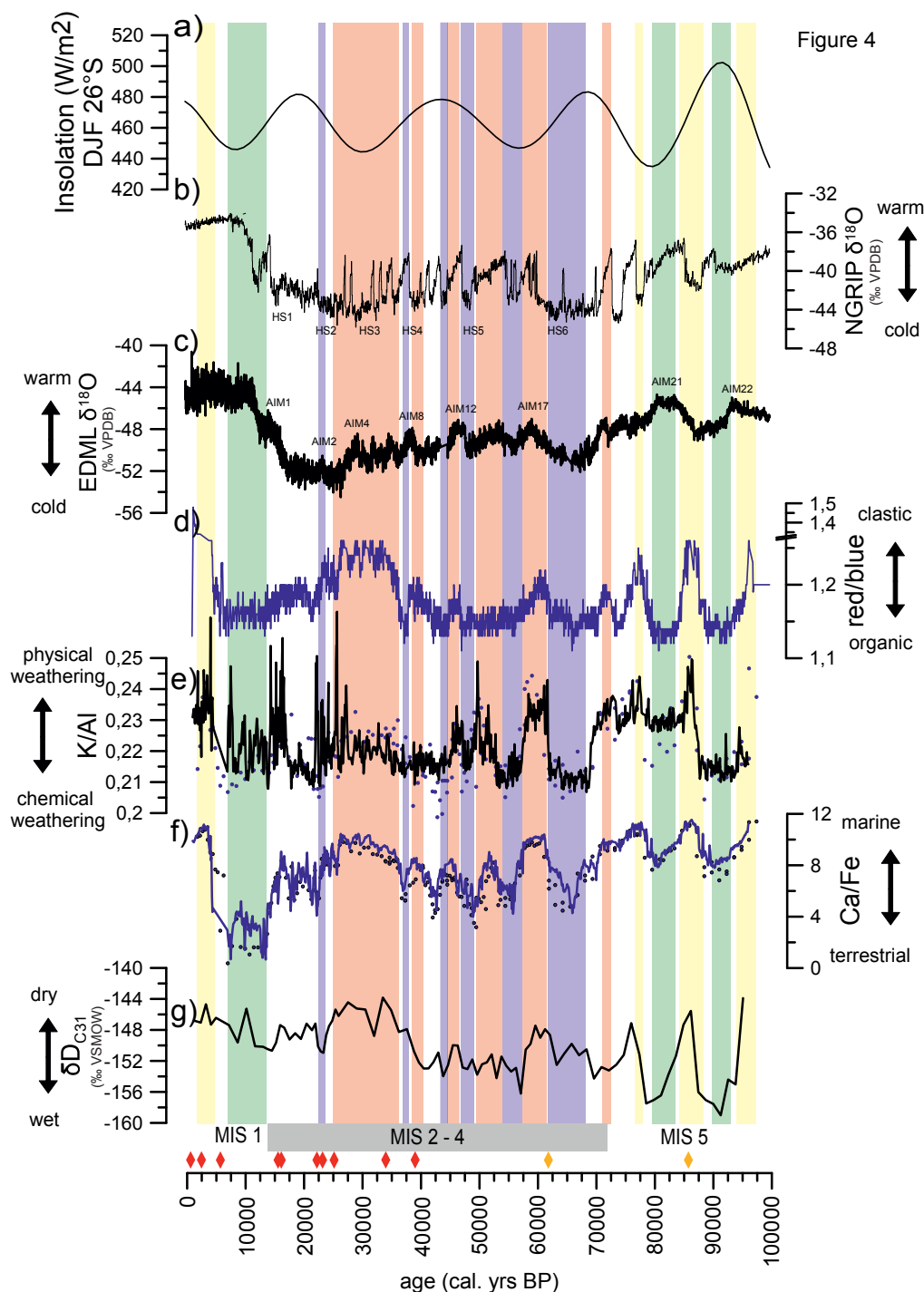
Fig. 4 Organic and inorganic down-core geochemistry (c-f: δD, red/blue, K/Al and Ca/Fe) of GeoB20616-1 as indicators for weathering type, fluvial input and aridity. Intervals identified as wet using these indicators are marked in blue or green, while wet phases are marked in red or yellow. Wet intervals marked in green are associated with southward shifts of the SHW and the South African high-pressure cell allowing for the SIOCZ and related rain bearing TTT to move over the study area during interglacials. In turn, wet intervals marked in blue are associated with northward shifts of the SHW related low pressure cells and/or southward shifts of the ITCZ during glacials. Arid phases during interglacials (marked in yellow) are related to northward shifts of the SHW as this induces the moisture-blocking effect of the South African high-pressure cell over the region. During glacials, however, southward shifts of the SHW are often associated with arid phases (marked in red) as the rain-bearing low pressure systems related to the SHW move south. XRF scanning data is marked as a line, whereas discrete XRF measurements are represented by points. Panel c represents the δD of the C_{31} n alkane in the unit ‰ VSMOW. For comparative purposes local insolation (Laskar, 2011) as well as Arctic and Antarctic ice core d[18]O records are plotted (NGRIP members, 2004; EPICA members, 2010). The most prominent AIM (Antarctic isotope maxima) and HS (Heinrich Stadial) events are named. The diamonds indicate C[14] dates (red) and δ^{18}O tie points (orange).
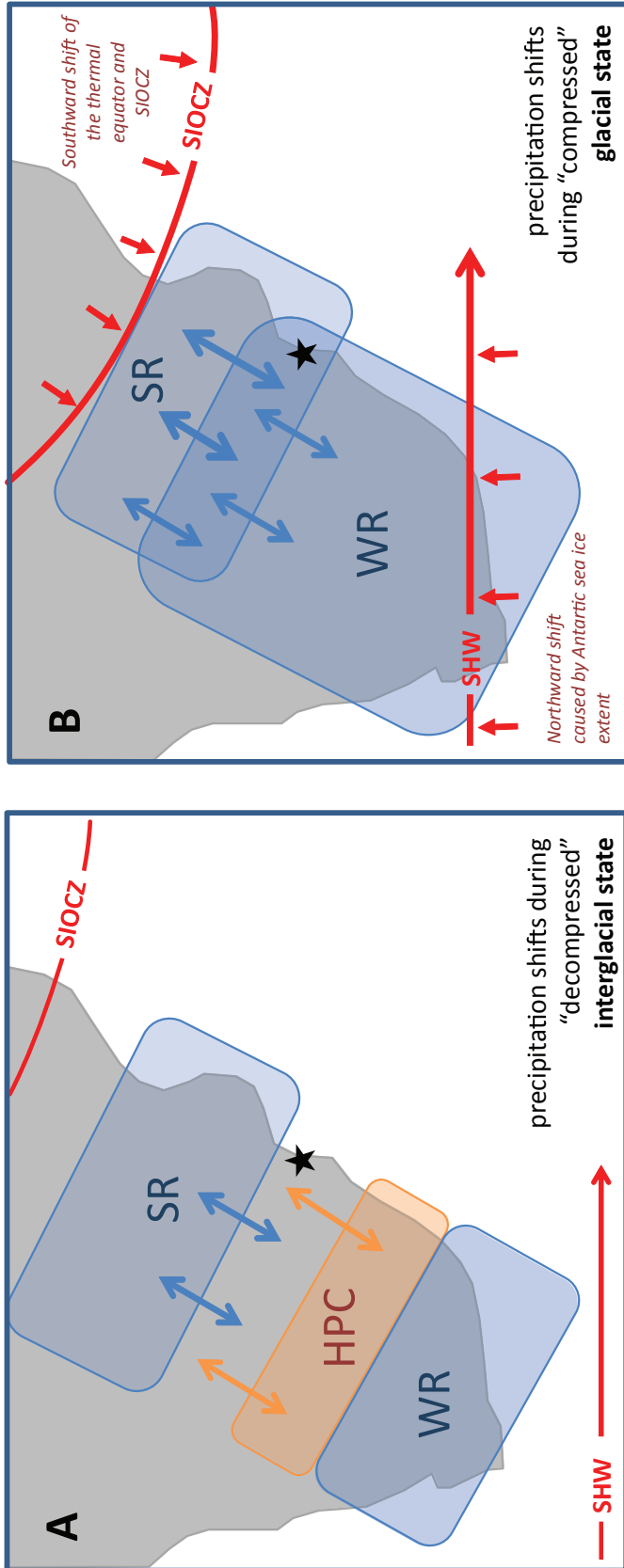
Fig. 5 Conceptual model of precipitation shifts during glacial vs. interglacial intervals. The blue shaded boxes indicate the locations of the major regional rain-bearing systems: i) the TTT moisture shifting with the SIOCZ and bearing summer rain (therefore marked as SR) ii) the low-pressure systems related to the SHW, bringing mainly winter rain (therefore marked as WR). The orange shaded box marks South African high-pressure cell (HPC) shifting with the SHW. The HPC blocks SIOCZ and TTT related moisture and therefore causes aridity. The arrows mark the millennial scale variability of the position of these systems over the study area which is marked by a star. Please note that the millennial scale variations that the region experiences differ in the interglacial state (box A) and the glacial state (box B) since the organization of the major climatic systems (marked in red) is different ("decompressed" vs "compressed"). The conceptualization for interglacial states presented in box A is based on a schematic model by (Miller et al., 2019b). In this "decompressed" state latitudinal shifts of the SHW indirectly control precipitation at our study site via the moisture blocking effect of the South African HPC: southward shifts of the SHW and HPC allow the SIOCZ related TTT to bring SR to our site, whereas northward movements block this SR moisture (Miller et al., 2019b). During the "compressed" glacial state (box B) the SHW related WR reaches much further north, directly influencing the study site. The SR, in turn is shifted southward and an HPC blocking effect is not noted at our site.

Table. 1 AMS radiocarbon analyses of material from core GeoB20616-1. The modelled ocean average curve (Marine13) (Reimer et al., 2013) was used for calibration and a local ΔR of 121±16 ^{14}C yr (Maboya et al. 2017) was applied. The ages were calibrated with Calib 7.1 software (Stuiver et al. 2018)

core	material	depth	lab nur	[14]C uncalib.	cal. age yrs BP		
		(cm)			-2s	+2s	median
GeoB20616-1	bulk	0.5	Poz-89C	1640 ± 30 BP	972	1168	1075
GeoB20616-1	*Globigerinoides ruber*	2	Poz-88€	2860 ± 90 BP	2262	2718	2473
GeoB20616-1	*Globigerinoides ruber*	52	Poz-89C	5860 ± 150 BP	5794	5796	6139
GeoB20616-1	*Globigerinoides ruber*	102	Poz-89C	14290 ± 200 BF	16063	17248	16648
GeoB20616-1	*Globigerinoides ruber*	152	Poz-89C	13960 ± 390 BF	15047	17400	16170
GeoB20616-1	*Globigerinoides ruber*	202	Poz-89C	19160 ± 200 BF	22002	22971	22511
GeoB20616-1	*Globigerinoides ruber*	252	Poz-88§	20370 ± 220 BF	23342	24413	23877
GeoB20616-1	*Globigerinoides ruber*	302	Poz-89C	22070 ± 220 BF	25365	26216	25826
GeoB20616-1	*Globigerinoides ruber*	352	Poz-88€	30850 ± 870 BF	32455	36152	34343
GeoB 20616-1	shell fragment	390	Poz-85C	35820 ± 520 BF	38724	41007	39859
GeoB 20616-1	gastropod	634	Poz-85C	>52000 BP	Date out of range		
GeoB 20616 -1	coral	664	Poz-85C	>48000 BP	Date out of range		